ON THE EFFECTS OF BINARY GAS ON SECOND-MODE

INSTABILITY

by

Arnav N. Prasad

A thesis submitted to the Faculty of the University of Delaware in partial fulfillment of the requirements for the degree of Honors Bachelor of Mechanical Engineering with Distinction

Spring 2020

ON THE EFFECTS OF BINARY GAS ON SECOND-MODE INSTABILITY
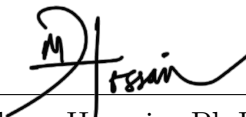
by

Arnav N. Prasad

I certify that I have read this thesis and that in my opinion it meets the academic and professional standard required by the University as a thesis for the degree of Bachelor of Mechanical Engineering.

Signed: _____

Joseph Kuehl, Ph.D.
Professor in charge of thesis

Approved: _____

Joseph Feser, Ph.D.
Committee member from the Department of Mechanical Engineering

Approved: _____

Zubaer Hossain, Ph.D.
Committee member from the Board of Senior Thesis Readers

Approved: _____

Michael Chajes, Ph.D.
Deputy Faculty Director, University Honors Program

ACKNOWLEDGMENTS

TABLE OF CONTENTS

LIST OF TABLES

LIST OF FIGURES

ABSTRACT

Sustained, reliable hypersonic flight has not yet been achieved, and has proven to be difficult for several reasons. One such reason is the prediction of transition — where the flow over the vehicle is no longer laminar, and is instead turbulent. Until this transition location can be reliably calculated, the design of hypersonic flight vehicles (in particular their control surfaces) will be difficult, if not impossible.

At the high air temperatures experienced during hypersonic flight, binary gases, namely oxygen (O_2) and nitrogen (N_2) are able to dissociate. The primary goal of this thesis is to understand what effect, if any, these dissociative "real gas" effects have on the second-mode instabilities of a hypersonic boundary layer. If it is found that the real gas effects make no significant difference to stability, then designing under an ideal gas approximation will be effective. On the contrary, if real gas effects greatly affect the instabilities, then they must be considered in the design of hypersonic vehicles.

Additionally, this thesis presents these differences in the context of the thermoacoustic interpretation of second-mode instability. The thermoacoustic interpretation describes possible reasons for why certain frequencies are less stable than others, as well as where the energy for the instability growth is provided. Once the profiles and instabilities for the ideal and real gas cases are determined, their alignment with this interpretation is be further analyzed.

Chapter 1

BACKGROUND

1.1 Hypersonic Flight

The realm of hypersonics refers to objects traveling at speeds higher than Mach 4 (that is, 4 times faster than the speed of sound) [1]. At sea level, this corresponds to speeds greater than 1.36 kilometers per second. The world has achieved hypersonic flight: Rockets re-entering the atmosphere regularly travel at Mach 25, and the Apollo missions which landed astronauts on the moon achieved an awe-inspiring Mach 36 [2]. Sustained, reliable, hypersonic flight, however, is a different story[1]. There have been several attempts to design and build hypersonic transport vehicles, primarily funded by U.S. Air Force and the U.S. Department of Defense [2]. Rather than taking shape as rockets, these vehicles look similar to traditional aircraft, and hope to take off and land like them too. Unfortunately, these projects are yet to come to fruition, ending typically in cancellation due to complexity in design [2]. In 2004, NASA tested their Hyper-X X43 Autonomous Hypersonic Vehicle. The goal of this program was to test 3 scramjet vehicles at Mach 7 and Mach 10, and collect data for comparison with wind-tunnel test conditions [3]. This generated a real-world dataset, for use in verification of both simulations and wind-tunnel scaled experiments.

At these high speeds, traditional aerodynamics (which have been studied in great detail) are no longer sufficient to predict the flow of fluid past a vehicle [4]. Instead, the analyses become more complex, and phenomena which don't play a role in lower-speed dynamics (for example, chemical reactions in the air) may become critical. Developing controlled, hypersonic flight has certainly proved difficult in the past — The X43 program mentioned earlier, for example only flew 3 missions. The first failed

catastrophically, lacking the flight surfaces necessary for sufficient control. The second and third missions succeeded, but managed powered flight for only approximately 11 seconds each [2].

So why pursue hypersonics at all? The field has drastic implications in multiple sectors, primarily defense and commercial air transport [4]. In those same X43 tests which lasted just over 10 seconds, the vehicles travelled 15 miles (Mach 6.83) and 20 miles (Mach 9.68) [3]. A hypersonic commercial transport could make the flight from New York to Los Angeles in just over an hour travelling at Mach 5 — compared to the 6 hour flight at subsonic aircraft speeds [4]. Clearly, the ability to traverse such great distances in small amounts of time will prove useful in defense applications as well. Finally, spacecraft undergoing atmospheric reentry commonly reach hypersonic speeds [2]. Deeper understanding of hypersonic flight will drastically improve chances of success in the critical, most dangerous part of spaceflight missions.

Studying and comprehending the instabilities in a hypersonic boundary layer will allow us to better predict where the flow transitions from laminar to turbulent. This "tripping" of the flow is attributed to several factors, but the asymmetric drag and the frictional heating taking place are some of the most crucial phenomena which still are not understood [5]. Knowing what types of flow are present at different points on a flight vehicle is crucial - without this knowledge, effective control surfaces cannot be designed, leading to catastrophic failure. Overall, understanding boundary layer instabilities will enable the design and production of hypersonic vehicles which are safer, reusable, and more economically viable.

1.2   Thermoacoustic Interpretation of Second-Mode instability

This thesis will focus on studying the effects of binary gas chemical reactions on second-mode instability in a Blasius boundary layer. Second-mode instability is a key driver of the laminar to turbulent flow transition for axisymmetric flow at Mach numbers of approximately 4 and greater, making it an important consideration when

designing a hypersonic vehicle [6]. These instabilities appear as a streamwise prop-
agating disturbance, with acoustic signatures in the ultrasonic range. Kuehl (2018)
proposes a new theory by which we can understand the fundamental dynamics of
second-mode instabilities, dubbed a 'thermoacoustic interpretation'.

In this theory, the instability is modeled as a thermoacoustic resonator, resonat-
ing in an "acoustic impedance well" formed within high-speed boundary layers. The
object wall has infinite acoustic impedance, and near the sonic line (where the velocity
is equal to the speed of sound, or M=1 [7]) a secondary peak in impedance is formed
by strong boundary layer density gradients. The low impedance section between them
is known as the "acoustic impedance well." The existence of this well is necessary to
maintain acoustic resonance which drives the second-mode instability[6]. Inside this
well, the second-mode appears as a quarter-wavelength standing wave which is driven
by thermoacoustic Reynolds stresses. Changing the shape or size of this impedance
well has a direct effect on the strength of the instability, resulting in different transition
locations.
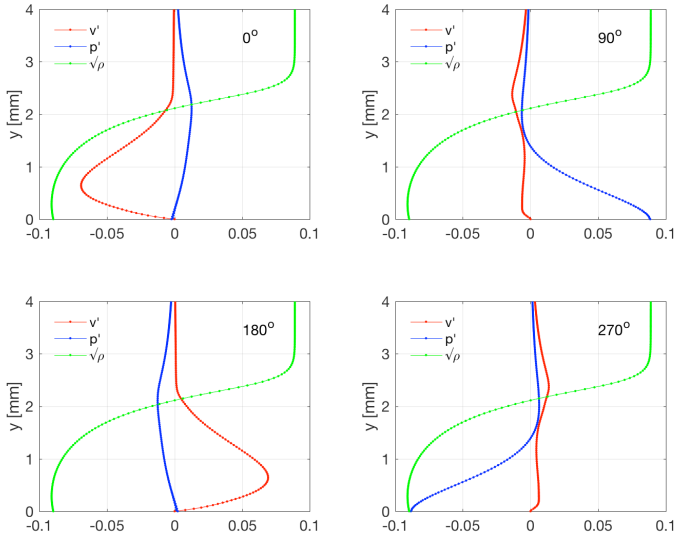
Figure 1.1: Phases of oscillation for a thermoacoustic second-mode instability in a
hypersonic boundary layer, reproduced with permission from Batista 2019.

1.3   Chemical Effects on Stability

Tumin, Ulker, and Klentzmann (2012) have shown that chemical reactions of a binary gas in a hypersonic boundary layer can alter the second-mode instability dynamics [8]. At the high temperatures associated with hypersonic flight (atmospheric re-entry, for example), air no longer behaves as an ideal gas [9]. Instead, there are vibrational excitations and gaseous dissociations taking place, which cause the ideal models to break down. The "real gas effects" tend to stabilize the first-mode instability (which is believed to be the supersonic extension of the viscous Tollmien–Schlichting instability), and destabilize the second-mode instability. Additionally, the inclusion of binary gas dissociation appeared to reduce the equilibrium wall temperature, under the assumption that the wall was adiabatic [8].

The selection of which species to model yields different results on stability. Oxygen, for example, has a lower dissociation energy than nitrogen — this tends to absorb energy fluctuations and increase the stability of the flow, whereas the same flow conditions modeled under a binary nitrogen species was less stable. This thesis focuses on both the oxygen and nitrogen binary gas models, in order to highlight the stability differences between chemically reactive and ideal-gas boundary layers. Klentzman and Tumin (2014) studied two cases: 1) the chemical reactions taking place were equilibrium, or 2) "non-equilibrium," the free stream was assumed to be a nearly-pure binary gas. In their research, they found that chemical equilibrium cases had been explored in depth, but the non-equilibrium cases would have a different, significant impact on stability [10]. In this thesis, we seek to extend their results in the context of thermoacoustic interpretation.

<div align="center">

Chapter 2

METHODOLOGY

</div>

2.1 Ideal Gas, Compressible Blasius Boundary Layer Calculations

In order to solve for the Blasius boundary layer profiles in an ideal gas, the following equations were solved. These equations were derived in [11], and are reproduced here with permission. First, there is the conservation of mass:

$$\frac{\partial \rho}{\partial t} + \nabla \cdot (\rho \mathbf{u}) = 0$$

Which can be rewritten as:

$$\frac{\partial \rho}{\partial t} + \left(\frac{\partial \rho u}{\partial x} + \frac{\partial \rho v}{\partial y} + \frac{\partial \rho w}{\partial z} \right) = 0 \tag{2.1}$$

Where ρ is the density, t is time, and u, v, and w represent the x, y, and z components of velocity, respectively. Next, the x-momentum equation, given in the compressible form:

$$\rho \left(\frac{\partial \mathbf{u}}{\partial t} + \mathbf{u} \cdot \nabla \mathbf{u} \right) = \nabla(-P + 2\mu e_{ij} + \lambda \nabla \cdot \mathbf{u}) \tag{2.2}$$

Here P is the thermodynamic pressure. μ is the first coefficient of viscosity, and λ is the second coefficient of viscosity. The strain rate tensor $e_{ij} = \frac{1}{2} \left(\frac{\partial u_i}{\partial x_j} + \frac{\partial u_j}{\partial x_i} \right)$. A Newtonian fluid is assumed. Lastly, the energy equation is derived, starting in the general form:

$$\rho \frac{De}{Dt} = \dot{Q} - \nabla \cdot \mathbf{u^2} - P(\nabla \cdot \mathbf{u}) + \phi$$

In this equation, e represents energy, $\dot{Q}$ is the heat generation, and ϕ is the viscous dissipation of the form

$$\phi = (2\mu + \lambda) \left[\left(\frac{\partial u}{\partial x} \right)^2 + \left(\frac{\partial v}{\partial y} \right)^2 + \left(\frac{\partial w}{\partial z} \right)^2 \right] + \mu \left[\left(\frac{\partial w}{\partial y} + \frac{\partial v}{\partial z} \right)^2 + \left(\frac{\partial w}{\partial x} + \frac{\partial u}{\partial z} \right)^2 + \left(\frac{\partial v}{\partial x} + \frac{\partial u}{\partial y} \right)^2 \right]$$
$$+ 2\lambda \left[\frac{\partial u}{\partial x} \frac{\partial v}{\partial y} + \frac{\partial u}{\partial x} \frac{\partial w}{\partial z} + \frac{\partial v}{\partial y} \frac{\partial w}{\partial z} \right]$$

When we assume that the fluid is an ideal gas and a Stokes fluid ($\lambda = -\frac{2}{3}\mu$), and we use Fourier's Law pertaining to heat conduction, this becomes:

$$\rho c_p \frac{DT}{Dt} = (\nabla \cdot k\nabla)T - P(\nabla \cdot \mathbf{u}) + \phi + \dot{Q} \tag{2.3}$$

The equations derived here have terms for all the spatial dimensions (x,y,z), as well as time (t). For this thesis, the flow was assumed to be steady state and two dimensional — that is, only varying in x (the streamwise direction) and y (the wall-normal direction), with $w = 0$. This simplifies the equations, removing terms with time variation (for example $\frac{\partial \rho}{\partial t}$ in equation 2.1), and dependence on w. The compressible Blasius boundary layer equations are listed below, reproduced from Kuehl (2018) [6].

$$f''' = \frac{g'f''}{g + C_1} - \frac{g'f''}{2g} - \frac{ff''(g + C_1)}{C_0 g^{1/2}} \tag{2.4}$$

$$g'' = \frac{g'^2}{g + C_1} - \frac{g'^2}{2g} - \Pr(\gamma - 1)M^2 f''^2 - \frac{\Pr f g'(g + C_1)}{C_0 g^{1/2}} \tag{2.5}$$

In the above equations, the following symbols are used:

$$f' = \frac{u}{U_e}, \quad g = \frac{T}{T_e}, \quad C_0 = \frac{C_\mu T_e^{1/2}}{\mu_e}, \quad C_1 = \frac{S}{T_e}, \quad C_\mu = \frac{\mu_{\text{ref}}}{T_{\text{ref}}^{3/2}}(T_{\text{ref}} + S)$$

Pr is the Prandtl number, $\frac{\nu}{\alpha}$, where ν is the kinematic viscosity, and α is the thermal diffusivity. U_e, T_e, μ_e correspond to the edge velocity, temperature, and dynamic viscosity, respectively. The *ref*-subscripted quantities represent reference quantities from Sutherland's Law, and S is the Sutherland temperature, which are all tabulated values. The system of differential equations 2.4–2.5 was solved using a numerical solver, outputting the profiles of velocity, density, and temperature within the boundary layer.

2.2 Chemically Reacting, Compressible Blasius Boundary Layer Calculations

In order to apply the chemistry effects to the boundary layer solution, the authors of Ref. [8] first solved the momentum (2.7) and continuity (2.6) equations. Afterwards, they separately solved the energy (2.9) equation, and compared it to the results of their species conservation (2.8) equation. The solution was iterated upon until desired convergence was reached, at which point the code outputs a set of profiles corresponding to the Blasius Boundary Layer solution.

In the code provided by Tumin [8], the reactions for either Nitrogen or Oxygen binary gas dissociation could be enabled, though not simultaneously. The wall (flat plate) could be specified as either adiabatic or held at a constant temperature, as well as non-catalytic or partially catalytic. The user specifies the length of the plate, which is the streamwise distance from the nose at which the profiles are generated. Additionally, the user specifies the free stream temperature, pressure, and velocity to set up the test conditions.

Tumin's code also works on an assumption of steady state, two-dimensional flow, neglecting crossflow ($w = 0$). This yields a similar equation for mass conservation:

$$\frac{\partial(\rho u)}{\partial x} + \frac{\partial(\rho v)}{\partial y} = 0 \tag{2.6}$$

The equation for x-momentum (from the compressible Navier-Stokes) is also similar, though written in a slightly different form:

$$\rho u \frac{\partial u}{\partial x} + \rho v \frac{\partial u}{\partial y} = \frac{dp_e}{dx} + \frac{\partial}{\partial y}\left(\mu \frac{\partial u}{\partial y}\right) \tag{2.7}$$

Here, p_e represents the edge pressure, which is the free-stream pressure just outside the boundary layer. The next equation used to compute the real gas Blasius boundary layer is the species conservation equation:

$$\rho u \frac{\partial c_s}{\partial x} + \rho v \frac{\partial c_s}{\partial y} = \frac{\partial}{\partial y}\left(\rho D \frac{\partial c_s}{\partial y}\right) + \dot{W}_s \tag{2.8}$$

In equation 2.8, c_s represents the concentration of species s. D is the binary diffusion coefficient, and $\dot{W}_s$ is the chemical source term for species s, given by $\dot{W}_s = M_s \frac{d[s]}{dt}$. In

the code provided, species s refers to either oxygen (O_2) or nitrogen (N_2). The final equation necessary is the energy conservation equation. This is quite different than the energy conservation equation for an ideal gas, and is given by:

$$\rho u \frac{\partial I}{\partial x} + \rho v \frac{\partial I}{\partial y} = \frac{\partial}{\partial y} \left[\frac{\mu}{Pr} \frac{\partial I}{\partial y} + \mu \left(1 - \frac{1}{Pr} \right) \frac{1}{2} \frac{\partial u^2}{\partial y} - \left(\frac{1}{Le} - 1 \right) \rho D \sum_s \frac{\partial c_s}{\partial y} \right] \quad (2.9)$$

Pr is the Prandtl number. D is the mass diffusivity of the flow, and Le is the Lewis number, $\frac{\alpha}{D}$. I represents the total enthalpy of the system, given by:

$$I = h + \frac{u^2}{2}$$
$$h = \sum c_s h_s$$
$$h_s = \int_0^T C_{ps} dT + h_s^0.$$

where C_{ps} is the specific heat and h_s^0 is the heat of formation of species s.

2.3 Linear Stability Theory

A stability analysis performed on the boundary layer profiles enables one to determine the shift from laminar to turbulent flow, allowing for the proper design of flight surfaces and vehicle geometry. To make such analyses possible, the normal mode concept is adopted. Using the normal mode concept, it is possible to calculate values for α, the wave number associated with a disturbance. The formulation for the stability analysis is given below.

The following equations (2.10 - 2.12) are the disturbance form of the Navier-Stokes equations for an incompressible flow. The LST code used in this thesis is designed for compressible flow, which is more realistic [12]. The equations used are similar to those for incompressible flow, with some additional terms not reproduced here. Additionally, these equations assume parallel flow, meaning that the velocity, density, and temperature profiles within the boundary layer are only a functions of the wall-normal distance y. This is valid to first order in the Taylor expansion sense, because the boundary layer is slowly varying [13]. The flow is also assumed to be uniform across the cross-section, so the z direction is disregarded.

8

Below, ϕ is a general variable which can represent ρ, u, v, T, and is broken into base state and disturbance terms:

$$\phi = \begin{Bmatrix} \rho \\ u \\ v \\ T \end{Bmatrix}, \phi(x, y, t) = \underbrace{\bar{\phi}(y)}_{basestate} + \underbrace{\phi'(x, y, t)}_{disturbance}$$

And adding the parallel flow assumption:

$$\bar{u}(y), \bar{v} = 0, \bar{p}(y)$$

Yields the 2D, parallel, incompressible flow equations of motion:

$$\frac{\partial u'}{\partial x} + \frac{\partial v'}{\partial y} = 0 \tag{2.10}$$

$$\frac{\partial u'}{\partial t} + \bar{u}\frac{\partial u'}{\partial x} + v'\frac{\partial \bar{u}}{\partial y} = -\frac{\partial p'}{\partial x} + \frac{1}{Re}\nabla^2 u' \tag{2.11}$$

$$\frac{\partial v'}{\partial t} + \bar{u}\frac{\partial v'}{\partial x} = -\frac{\partial p'}{\partial y} + \frac{1}{Re}\nabla^2 v' \tag{2.12}$$

The Navier-Stokes disturbance equations yield a separable solution, of the form $\phi'(x, y, t) = \hat{\phi}(y)e^{i\alpha x - i\omega t}$[14]. Here, $\hat{\phi}(y)$ is a complex function, and represents the shape of the wave. This thesis focuses on the spatial stability theory, and the wave number α. α is taken to be a complex number, $\alpha = \alpha_r + i\alpha_i$. ω is a parameter, the non-dimensional frequency of the disturbance. This was specified each time the stability code was run. The growth rate of the disturbance relating to this wave number is given by $e^{i\alpha x}$, written explicitly in complex form by $e^{i\alpha_r x - \alpha_i x}$ [14]. The real part of this expression now depends on α_i, and the streamwise distance x. As x increases (traveling downstream), the excitation will diminish if α_i is positive, and grow if α_i is negative. Therefore, a negative value of α_i corresponds to a mode with a positive growth rate — an unstable mode. Assuming

9

this disturbance form, the problem reduces to a generalized eigenvalue problem, which is solved in Matlab.

The equations above are formulated into a matrix, and then solved using an eigenvalue solver. The boundary conditions assumed [13] are:

- no-slip, impenetrable wall $(u\big|_{y=0} = v\big|_{y=0} = 0)$

- density (ρ) continuity

- Temperature is specified (either a constant wall temperature or adiabatic)

- Disturbances decay far away from the wall $(\rho', u', v', T' \xrightarrow[y\to\infty]{} 0)$

As this system is solved numerically, we get a discretized representation of both the discrete and continuous solution spectra. The discrete spectrum is associated with bound states of a system, whereas the continuous spectrum represents unbounded states. When plotted, (figure 2.1), the discrete points can be picked out, as they do not fit the "trends" of the continuous points. The focus of this thesis is the second-mode instability, which is contained in the discrete spectrum.
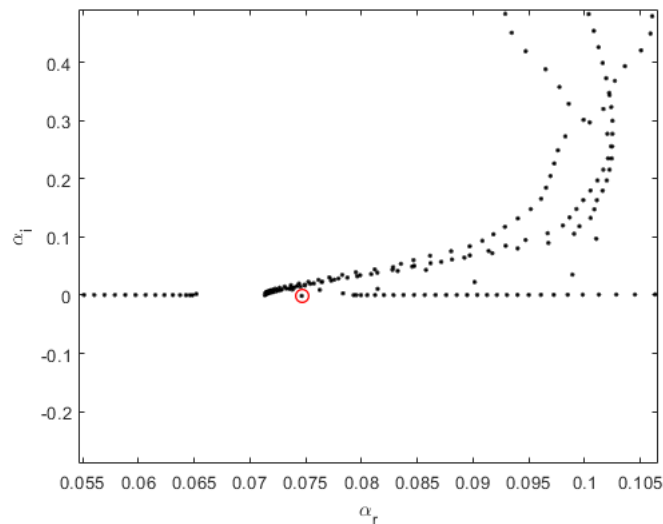

Figure 2.1: An example spectrum output from the linear stability code.

This spectrum was obtained from running an adiabatic test condition (see Chapter 3 for more information). The point circled in red is one of the discrete solutions,

found to correspond with the slightly unstable second-mode in this case. To validate that the selected point is, in fact, a second mode, one can plot the $u(y)$ and $v(y)$ velocity functions associated with this eigenvalue. The functions corresponding to a discrete mode have a distinct shape, and are smooth.The continuous spectrum is often subject to greater amounts of computational noise, and, as a result, can have shape functions which are clearly not physically representative. An example comparing two such functions is shown in figure 2.2, with boundary layer profiles evaluated at x = 0.1m. The horizontal axis is $|u|$, while the vertical axis is y, the wall-normal distance, nondimensionalized by the boundary-layer length scale (bL).

(a) $u(y)$, Discrete, Second-Mode   (b) $u(y)$, Computational Mode
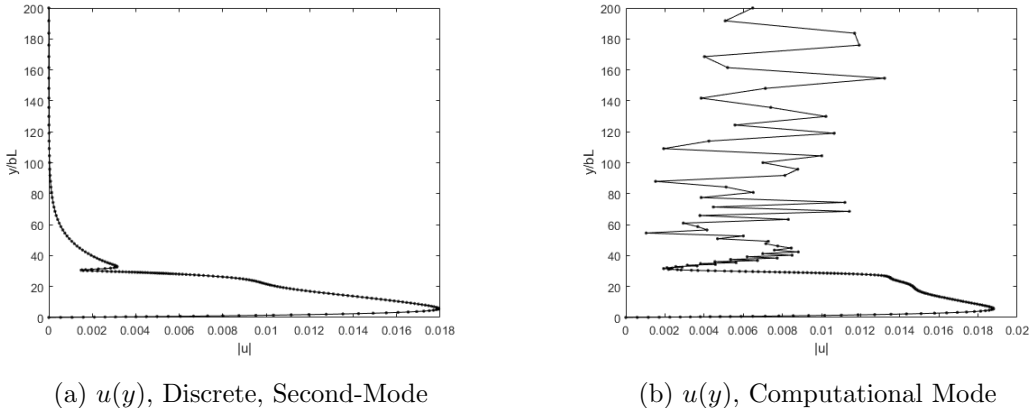
Figure 2.2: Shape function plots corresponding to a discrete, second-mode (left) and a computational mode (right).

Something of note is the lack of any chemistry-related terms in the Linear Stability formulation. Klentzmann and Tumin (2013) found that when considering the stability of second modes in a hypersonic boundary layer, the chemical terms could be neglected from the stability calculation, as they have no significant effect on the stability results [15]. Instead, the chemistry only needs to be accounted for in the base state itself, used to generate the Blasius boundary layer profiles that is then analyzed for instability.

Chapter 3

RESULTS

3.1   Test Conditions

To compute the chemical and ideal gas Blasius boundary layer profiles, a set of "test conditions" was prescribed. This was broken into two parts: the parameters which were fixed, and the parameters which were varied.

Constant Parameters:

- Mach Number = 10
- T_e = 230K
- P_e = 0.017atm
- x = 0.1m

These parameters correspond to the atmospheric conditions at 30 kilometers above sea level, in alignment with Ref. [16]. 30 kilometers was used in the HIFiRE project, as a representative altitude for hypersonic flight experiments [17].

Varied Parameters:

- Wall Condition: Adiabatic, Constant Temperature
- Wall Temperature: 2000K, 5500K (for Constant Temperature cases)
- Air Properties: Ideal Gas, O_2 dissociation enabled, N_2 dissociation enabled.

At each of the three wall conditions, the boundary layer profiles were plotted.

3.2 Boundary Layer Profiles

(a) Horizontal Velocity

(b) Temperature

(c) Density (Nondimensionalized by Edge Density)
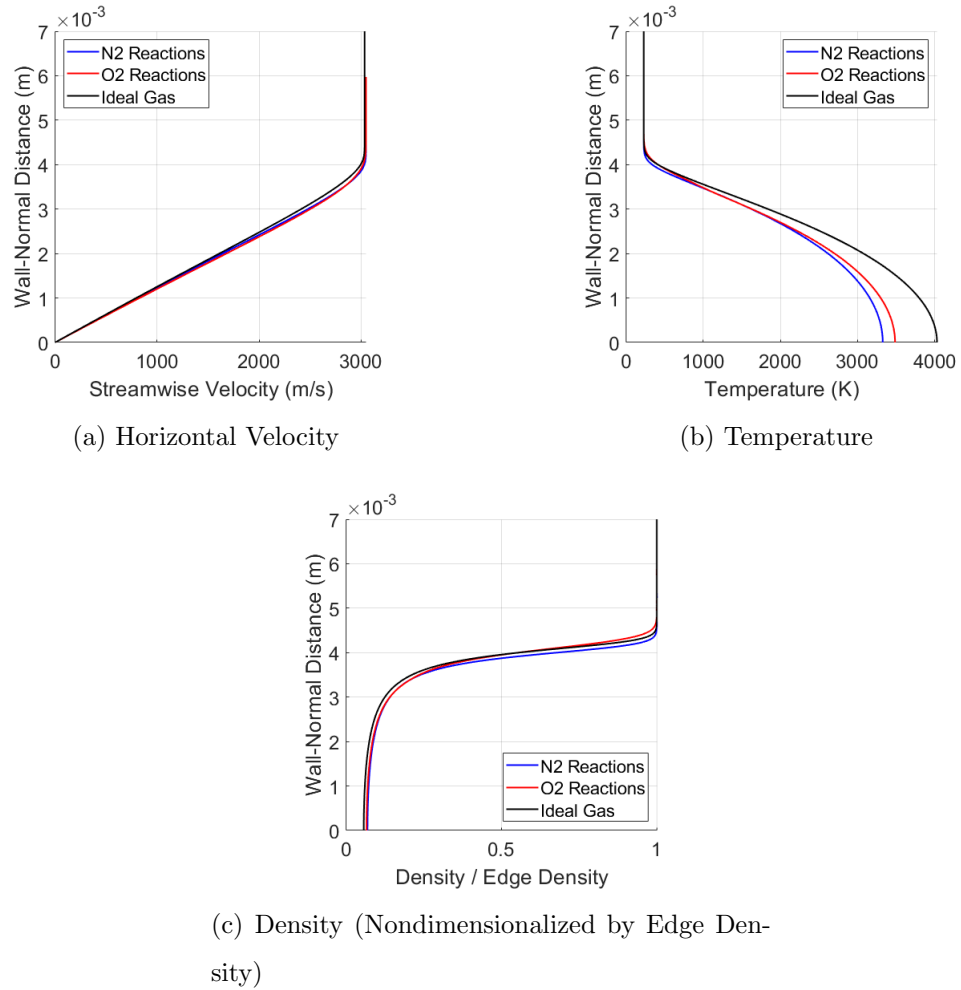
Figure 3.1: Horizontal Velocity, Temperature, and Density profiles for the Adiabatic Wall, plotted against the Wall-Normal distance.

From the Adiabatic case, the wall temperature is around 3500-4000K, due to frictional heating. This determined the two other test cases at constant wall temperature: One at 2000K (actively cooled wall), and the other at 5500K (actively heated wall). This case also shows an interesting effect of the chemical reactions taking place: the gaseous dissociations and recombinations work to lower the wall temperature [8].

(a) Horizontal Velocity

(b) Temperature

(c) Density (Nondimensionalized by Edge Density)

Figure 3.2: Horizontal Velocity, Temperature, and Density profiles for the actively cooled wall ($T_{wall} = 2000K$), plotted against the Wall-Normal distance.

Considering the cooled wall temperature profile, the system doesn't reach the location where gaseous dissociation is prevalent (>3000K)[8]. As such, the profiles generated for the ideal gas, O_2 reactions, and N_2 reactions are all quite similar.

(a) Horizontal Velocity
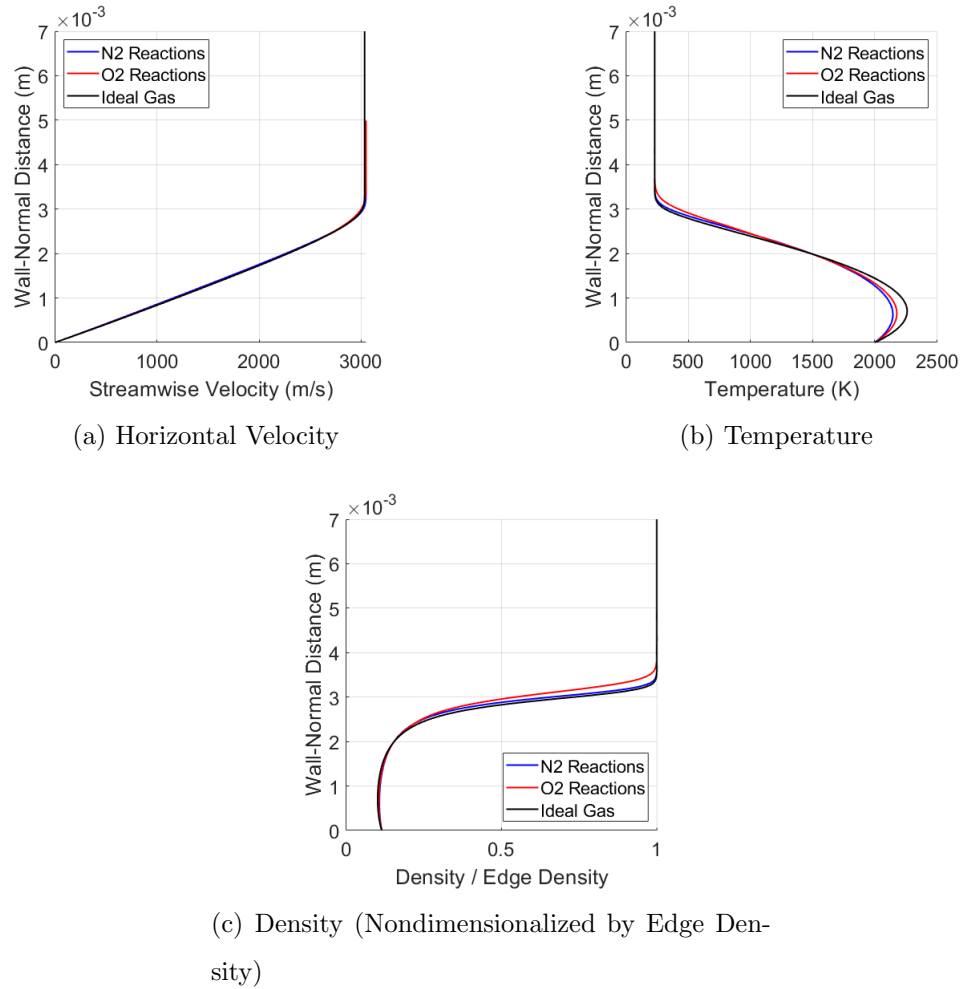
(b) Temperature

(c) Density (Nondimensionalized by Edge Density)
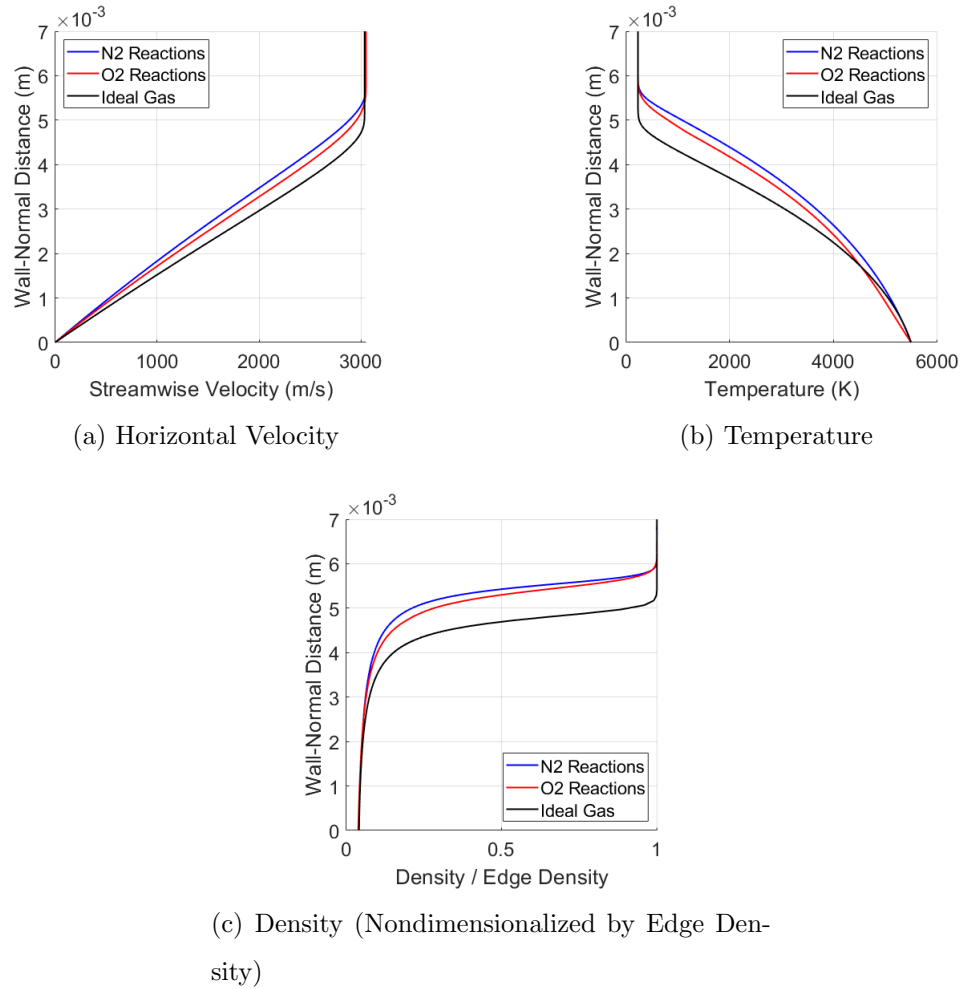
Figure 3.3: Horizontal Velocity, Temperature, and Density profiles for the actively heated wall ($T_{wall} = 5500K$), plotted against the Wall-Normal distance.

In the actively heated wall case, both oxygen and nitrogen dissociations are prevalent at the boundary layer temperatures [8]. This has a pronounced effect in separating the ideal and real gas boundary layers.

3.3 Instability Envelope Plots

After the boundary layer profiles were computed, they were analyzed for instabilities (see section 2.3 for details). The linear stability code was run at a "sweep" of specified frequencies (nondimensionalized to ω), until the second mode crossed from unstable to stable (α_i moved from negative to positive). This process resulted in the following three "instability envelopes" — frequencies at which the boundary layer was unstable.

(a) Adiabatic Wall

(b) Active Cooling ($T_w = 2000K$)

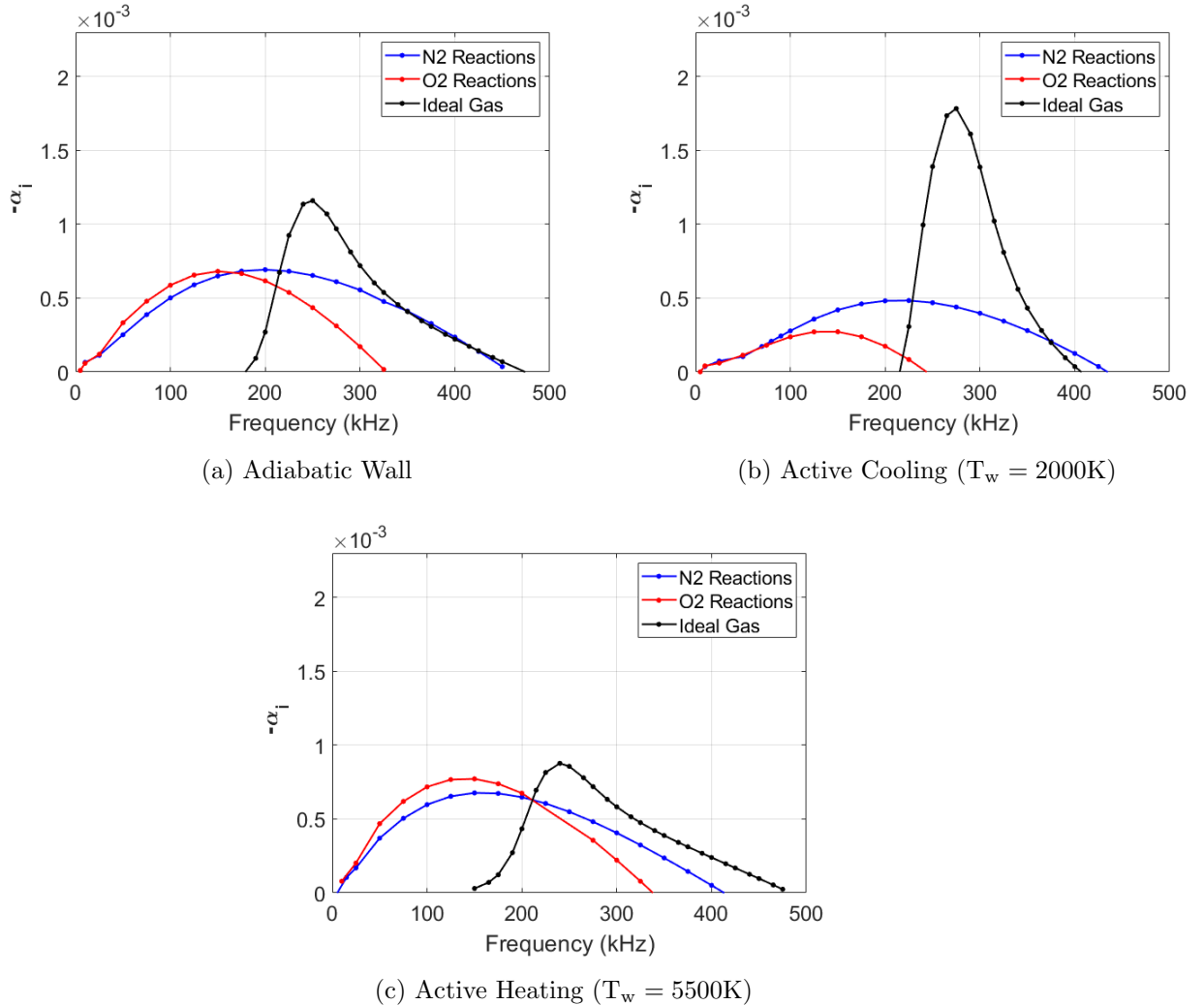(c) Active Heating ($T_w = 5500K$)

Figure 3.4: Instability Envelope Plots for each of the three wall test conditions. $-\alpha_i$ has been plotted, to make the plot more easily understandable. Run at x = 0.1 meters.

16

3.4 Discussion of Results

3.4.1 Theoretical Analysis

As stated earlier in section 1.2, using the thermoacoustic representation of second mode instabilities, the stability is analyzed as if it were a wave trapped in an acoustic impedance well. This impedance well is formed by two "walls": one being the physical wall of the flat plate, and the other is the sharp density gradients which form in the boundary layer (this is the point where the density profile is almost flat). Consistent with the properties of standard waves, if the distance is larger, the resonance frequency is lower, and vice versa. So one possible reason for the shift of the instability envelope to lower frequencies is the increase in height of the boundary layer. Another consideration is the local speed of sound in the boundary layers. The instabilities propagate at the speed of sound. Therefore, a lower local speed of sound will lead to lower frequencies being unstable, shifting the envelope to the left.

Looking over the density profiles and local speed of sound plots provides a qualitative explanation as to why the instability plots shift. In order to quantify this, the metric used was the average local speed of sound in the boundary layer divided by the boundary layer height ($k = \frac{\bar{a}}{\delta}$). This metric provides us with a numerical value, which we can relate to the expected peak frequency. The boundary layer height was taken to be the point at which the density profile has an inflection point, or a zero-valued second derivative. The local speed of sound $a = \sqrt{\gamma R T}$, where $\gamma = \frac{c_p}{c_v} = 1.4$ and R is the individual gas constant, taken as 288.7 for an ideal gas, and calculated by the chemically reacting boundary layer code [8] for the real gas cases. Then, the average local speed of sound $\bar{a}$ is given by

$$\bar{a} = \frac{1}{\delta} \int_0^\delta \sqrt{\gamma R T} \mathrm{d}y$$

Furthermore, when considering a real gas, γ and R could not be set as constants. They were found by the following calculations:

$$\gamma = \frac{C_p}{C_v}, \gamma_{air} = 1.4, \gamma_{gas}(y) = \frac{X_{dia}(y) * C_{p,dia} + X_{mono}(y) * C_{p,mono}}{X_{dia}(y) * C_{v,dia} + X_{mono}(y) * C_{v,mono}}$$

where X represents the mass fraction of the species. The subscripts *dia* and *mono* refer to the diatomic and monoatomic gases, respectively (O_2 and O, for example). Table 3.1 lists the formulas to find C_p, C_V as a function of R_{gas} for diatomic and monoatomic gases.

	Diatomic	Monoatomic
C_p	$\frac{7R_{gas}}{2}$	$\frac{5R_{gas}}{2}$
C_v	$\frac{5R_{gas}}{2}$	$\frac{3R_{gas}}{2}$

Table 3.1: Formulas to find C_p,C_v from R_{gas}, the specific gas constant, for diatomic and monoatomic gases.

The code from Tumin [8] outputs the mass fraction of each species, as well as $R_{gas}/R_{gas,edge}$, as functions of the wall-normal distance. $R_{gas,edge}$ is also provided, so C_p and C_v can be calculated along the wall normal distance as well.

To see if the stability results calculated are consistent with the thermoacoustic interpretation of second mode instabilities, each of the three test cases is analyzed in further detail.
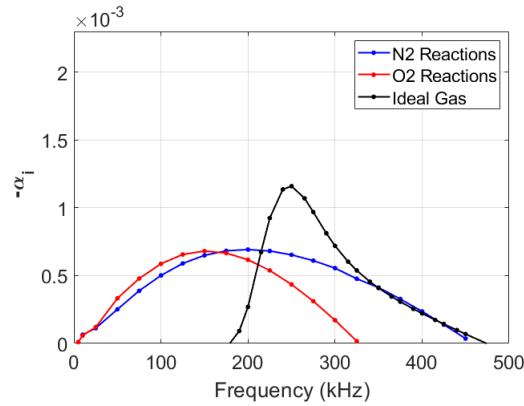
3.4.2 Adiabatic Wall
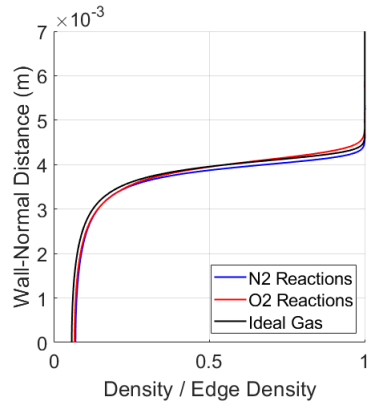
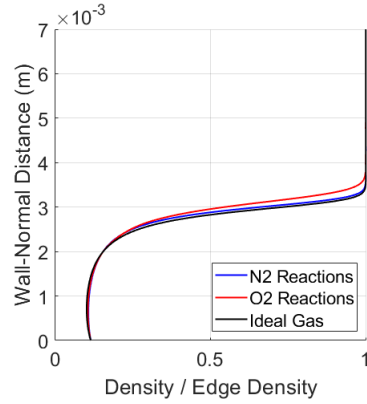(a) Density (Nondimensionalized by Edge Density)
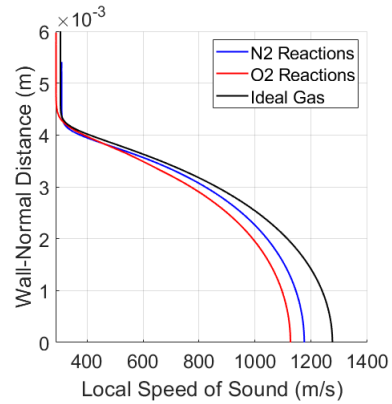
(b) Local Speed of Sound

(c) Instability Envelope

Figure 3.5: Density profile, local speed of sound profile, and instability envelope for the Adiabatic case.

As seen in figure 3.5a, the density profiles for all three gases are quite close. While the Nitrogen Reaction boundary layer appears to be the smallest, no clear, qualitative interpretation is gained. However, the local speed of sound plots (b) align with the theoretical predictions. The speed of sound is the largest for the ideal gas, then slower for the nitrogen reactions, and then slower still for the oxygen reactions. This matches the instability envelopes (c), where the ideal gas "peaks" at the highest frequency, followed by the nitrogen case and then the oxygen case.

Using our pre-described metric for comparison, $k_{O_2} = 2.26 \times 10^5$, $k_{N_2} = 2.45 \times 10^5$, and $k_{Id} = 2.55 \times 10^5$. Again, this lines up with the produced instability envelope plot, as the lower k predicts a lower peak frequency of instability. The value of k_{Id} also matches up with the frequency corresponding to the peak in the ideal gas instability envelope, but the same cannot be said for the real gas cases.

3.4.3 Actively Cooled Wall ($\mathrm{T_{wall}} = 2000K$)

(a) Density (Nondimensionalized by Edge Density)

(b) Local Speed of Sound

(c) Instability Envelope

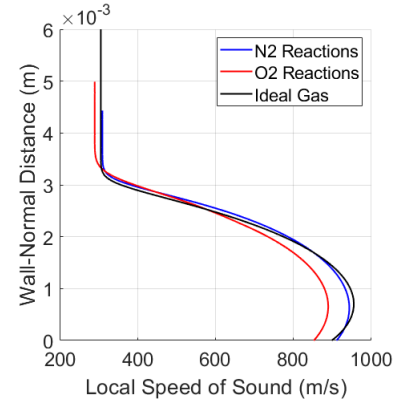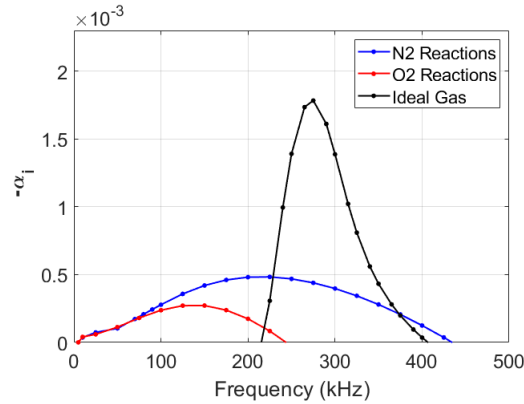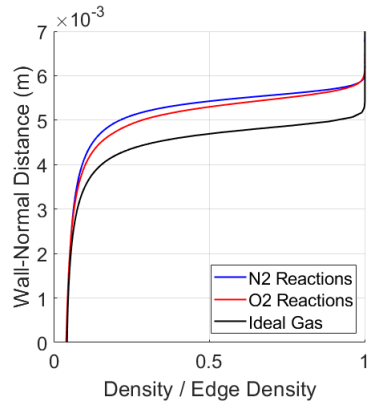Figure 3.6: Density profile, local speed of sound profile, and instability envelope for the Actively Cooled ($\mathrm{T_{wall}} = 2000K$) case.

In the density plot for the cooled wall case (fig. 3.6a), the oxygen reaction case has the largest boundary layer height. The nitrogen and ideal gas cases are barely separated. Moving to the speed of sound profiles (b), it is again evident that the oxygen reaction case has the lowest speed of sound. The profiles for the nitrogen and ideal gas case are again similar, though the ideal gas case is slightly faster. These profiles physically make sense — Nitrogen requires higher temperatures to dissociate than oxygen. Therefore, when the wall is cooled, the nitrogen is less able to dissociate, acting more like an ideal gas. The qualitative analysis of the density and speed of sound profiles agree with what is seen in the instability envelope plots (c), with the ideal gas being at the highest frequencies, followed by nitrogen, and lastly oxygen.

Numerically, the numbers for comparison are $k_{O_2} = 2.49 \times 10^5$, $k_{N_2} = 2.75 \times 10^5$, and $k_{Id} = 2.75 \times 10^5$. The values of k for nitrogen and the ideal gas are identical, and higher than the metric value for oxygen, even though all three peaks appear to be quite evenly spaced in frequency. At a low wall temperature, this actually can be explained: nitrogen reactions are minimized, effectively becoming an ideal gas, whereas oxygen reactions are still able to take place. What is curious, however, is the even separation in peak frequencies for all three profiles on the envelope plot. Further investigation may explain this discrepancy. Once again, the metric is an accurate prediction for the peak instability frequency for the ideal gas, but not for the real gases.

3.4.4   Actively Heated Wall ($T_{wall} = 5500K$)

(a) Density (Nondimensionalized by Edge Density)
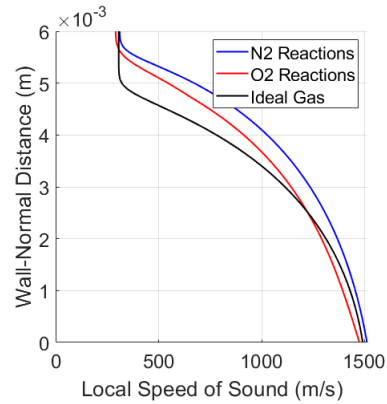
(b) Local Speed of Sound
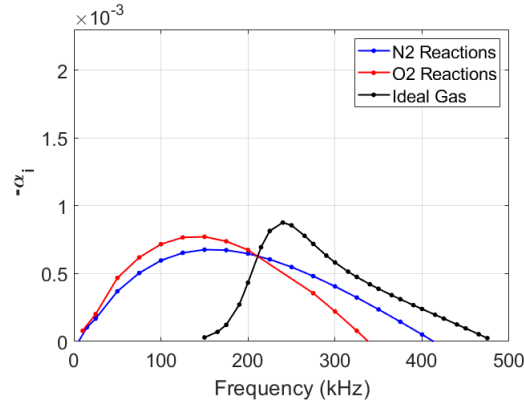
(c) Instability Envelope

Figure 3.7: Density profile, local speed of sound profile, and instability envelope for the Actively Heated ($T_{wall} = 5500K$) case.

The density profiles for the actively heated case (3.7a) show that the ideal gas case has a significantly lower boundary layer than the real gas cases. However, considering the instability envelopes in (c), it's evident that the profile for the ideal gas peaks only slightly higher than the two real gases. To explain this, one can examine the local speed of sound profiles (b). Here, both the real gases generate a higher speed

of sound than the ideal gas. This shifts their instability envelopes towards the higher frequency range, moving them closer to that of the ideal gas case.

Using the numerical metric once again, $k_{O_2} = 2.07 \times 10^5$, $k_{N_2} = 2.14 \times 10^5$, and $k_{Id} = 2.45 \times 10^5$. The values for oxygen and nitrogen reactions are quite close, and the peaks of their instability profiles appear quite close together as well. The value for the ideal gas is higher, and the instability profile is shifted to the higher frequency range as expected. The metric produces an accurate prediction of the peak frequency for the ideal gas instability.

3.4.5   Instability Growth Rate

The thermoacoustic interpretation for second-mode instability expects the source term for these thermoacoustic resonators to be the Reynolds stresses in the boundary layer. The acoustic energy equation is given in Kuehl 2018 [6], assuming an inviscid flow:

$$\underbrace{\frac{1}{2}\rho\frac{\mathrm{D}u^2}{\mathrm{D}t} + \frac{1}{2\rho c^2}\frac{\mathrm{D}P^2}{\mathrm{D}t}}_{\text{energy}} + \underbrace{\nabla \cdot (Pu)}_{\text{div. acst. pwr.}} = 0 \tag{3.1}$$

In equation 3.1, $u^2 = u^2 + v^2$, where u, v are the streamwise and wall-normal components of velocity, respectively. $c = \sqrt{\gamma P/\rho}$ is the speed of sound, where $\gamma = c_p/c_v$. P is pressure, and ρ is density. Furthermore, Kuehl derives the one-dimensional, ideal gas, inviscid, cycle-averaged disturbance energy acoustic equation to be

$$\frac{D\langle e \rangle}{Dt} = -\left[\left\langle \frac{d}{dy}\left(\bar{\rho}T'v'\right)\right\rangle + \left\langle \frac{d}{dy}\left(\bar{T}\rho'v'\right)\right\rangle\right] \tag{3.2}$$

where

$$\langle e \rangle = \frac{1}{2}\rho_e \left\langle \boldsymbol{u}'^2 \right\rangle + \frac{1}{2\rho_e c^2}\left\langle P'^2 \right\rangle$$

is the disturbance energy norm. From equation 3.2, it is evident that the thermoacoustic disturbances will grow when the thermoacoustic Reynolds stresses (in angle brackets) are negative. For viscous flow, the viscous Reynolds stresses must also be accounted for in equations 3.1 and 3.2, adding several additional terms which are not reproduced here. One such viscous Reynolds stress term, $u'v'\frac{\partial \bar{u}}{\partial y}$, is believed to be the

energy source for the first-mode instability, and so was the term chosen to represent the viscous Reynolds Stress.

As the disturbances grow in areas of negative thermoacoustic Reynolds stress, it follows that the more negative the Reynolds stresses are, the larger the instability growth rate should be. To analyze this theory further, the thermoacoustic and viscous Reynolds stresses for each wall case are given.

Adiabatic Wall

(a) Ideal Gas　　(b) N_2 Reactions　(c) O_2 Reactions
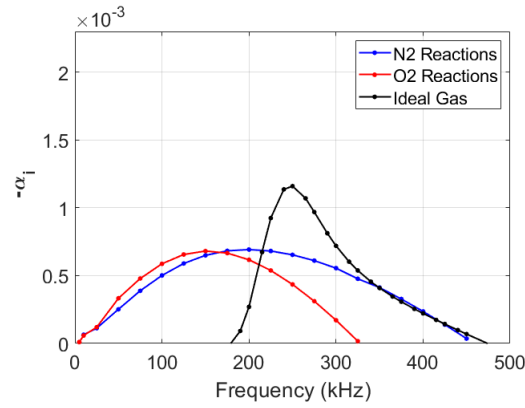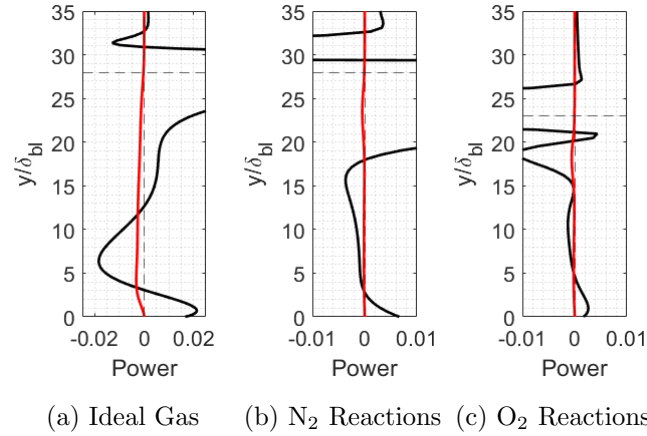

(d) Instability Envelope

Figure 3.8: Reynolds Stress Plots for the Adiabatic case. The black line represents the divergence of acoustic power (thermoacoustic Reynolds stress) and the red line shows the viscous Reynolds stress. Both are plotted in power per unit volume. The horizontal, dashed line represents the boundary layer height. Each stress was calculated at the corresponding peak unstable frequency.

In the instability envelope, the ideal gas peak has the largest magnitude. The nitrogen and oxygen peaks are lower, and fairly equal. This trend can also be seen in the Reynolds stress plots, when studying the thermoacoustic Reynolds stress (black). The ideal gas has a large negative region, while the nitrogen and oxygen reaction cases

are less so. However, this trend only holds if we analyze the curves from the middle of the boundary layer downwards.

Actively Cooled Wall ($T_{wall} = 2000K$)

(a) Ideal Gas   (b) N_2 Reactions   (c) O_2 Reactions

(d) Instability Envelope
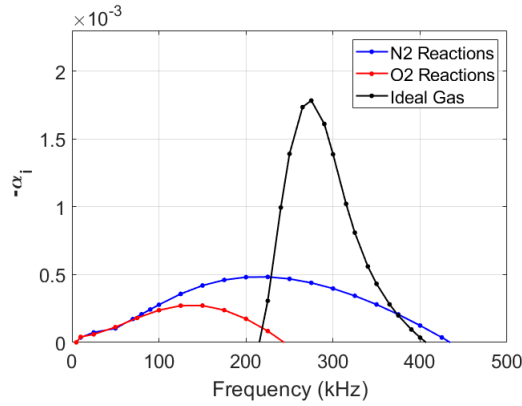
Figure 3.9: Reynolds Stress Plots for the Actively Cooled ($T_{wall} = 2000K$) case. The black line represents the divergence of acoustic power (thermoacoustic Reynolds stress) and the red line shows the viscous Reynolds stress. Both are plotted in power per unit volume. The horizontal, dashed line represents the boundary layer height. Each stress was calculated at the corresponding peak unstable frequency.

For the cooled wall case, analyzing the curves from the middle of the boundary layer downwards yields results consistent with the instability envelopes. The ideal

gas peak is significantly higher than the two real gas cases — while the Reynolds stress curves may look similar, note that for the ideal gas, the scale is one order of magnitude larger. The nitrogen and oxygen plots appear to have equal net-negativity, and their peaks do appear similar in magnitude. However, further analysis is necessary to determine why the Reynolds stress plots look similar, while the instability profiles have different peak magnitudes.

Actively Heated Wall ($T_{wall} = 5500K$)

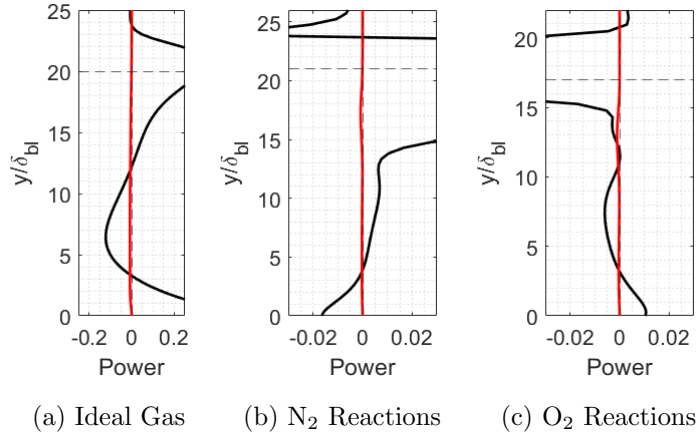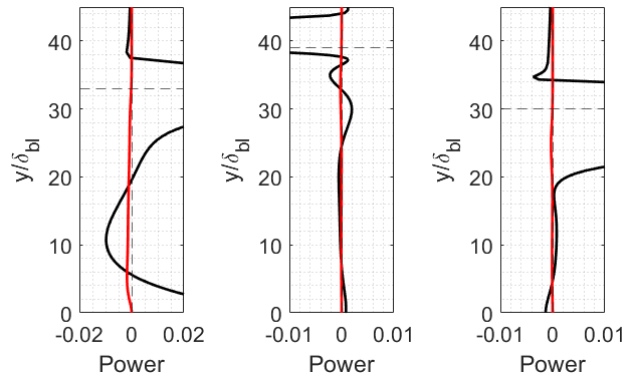(a) Ideal Gas   (b) N_2 Reactions (c) O_2 Reactions

(d) Instability Envelope

Figure 3.10: Reynolds Stress Plots for the Actively Heated ($T_{wall} = 5500K$) case. The black line represents the divergence of acoustic power (thermoacoustic Reynolds stress) and the red line shows the viscous Reynolds stress. Both are plotted in power per unit volume. The horizontal, dashed line represents the boundary layer height. Each stress was calculated at the corresponding peak unstable frequency.
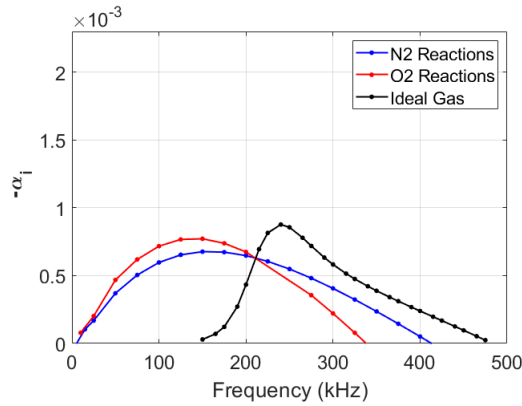
For the heated wall case, all three peaks in the instability envelope plot have comparable magnitudes. Analyzing from the middle of the boundary layer downwards, we do see that the average values of the thermoacoustic Reynolds stress curves are similar — ever so slightly negative. An interesting point, however, is that in this case,

the oxygen and nitrogen instability envelopes have peaks that are greater in magnitude than in the actively cooled case. But, the Reynolds stress plots show larger negative regions in the actively cooled case! While the trend of negative area to peak instability strength has held in each of the three cases, cross-comparing raises questions.

While trends have been found between the thermoacoustic Reynolds stress and the instability growth rate, it is evident that further study must be performed to thoroughly understand what the energy source term is for the instabilities. There seems to be promise in analyzing the thermoacoustic Reynolds stresses as one factor, but more sources are probably present. Additionally, to find such a trend, only the inner portion of the boundary layer was considered. The thermoacoustic stress appears to reach large amplitudes near the outer edge of the boundary layer, which has not yet been explained. This is a recommended line of further investigation.

Chapter 4

CONCLUSIONS AND FUTURE WORK

Overall, it is evident that the inclusion of real gas effects modifies the stability of a hypersonic boundary layer. More specifically, the dissociation of oxygen (O_2) and nitrogen (N_2) gases shifts the perceived instabilities into a lower frequency range than observed in an ideal gas. Additionally, the inclusion of such real gas effects decreases the instability growth rate.

Sufficient explanations for the frequency shifting of the instability envelopes has been found, attributed to both the boundary layer height and the local speed of sound in the boundary layer. The local speed of sound modifies how quickly the instability can propagate. The distance between the physical wall and the sharp boundary layer density gradients dictates the size of the acoustic impedance well, and like a typical oscillation, a larger distance leads to lower frequency resonance. More work is necessary to properly predict the peak instability growth rates — the metric used in this thesis, $\frac{\bar{\alpha}}{\delta}$, generally corresponded to the relative peak frequency in each case, but was not always an accurate indicator. Furthermore, the metric was unreliable in predicting the frequency at which the peak would occur for the chemically reacting cases, but successful in the ideal gas cases, which prompts investigation.

The thermoacoustic Reynolds stresses present in the boundary layer do appear to be a source of energy for the thermoacoustic resonators believed to be the second-mode instabilities. As expected, large, negative Reynolds stresses corresponded to relatively larger magnitudes of instability growth. However, more factors must be involved, as this was not a strong correlation. Our analysis focused on the center section of the acoustic impedance well, neglecting edge effects. These edge effects may change the Reynolds stress results, warranting further study. It is also evident that the

30

term chosen in this thesis to represent the viscous Reynolds stresses was not sufficient to explain the varying instability strengths — More terms from the viscous energy disturbance equation must be included.

In summary, this thesis was able to produce results similar to what was achieved by Tumin, Ulker, and Klentzmann in Ref. [8], contrasted with the results using an ideal gas approximation. The discrepancies were explained in the context of the thermoacoustic interpretation of second-mode instabilities. General trends that aligned with the thermoacoustic interpretation were found, but further work is still necessary to verify how the thermoacoustic resonator model is altered by finite rate chemistry.

REFERENCES

[1] Mark Lewis. Hypersonic Flight: Progress and Challenges on the Way to High Mach Systems. AIAA Presentation, 2018.

[2] John D. Anderson. *Hypersonic and High-Temperature Gas Dynamics*. American Institute ofAeronautics and Astronautics, Inc., second edition, 2006.

[3] Charles R. McClinton, Vincent L. Rausch, Luat T. Nguyen, and Joel R. Sitz. Preliminary X-43 flight test results. *Acta Astronautica*, 57(2-8):266–276, 2005.

[4] Armani Batista. *Fluid Dynamics Numerical Modeling of Second-Mode Instability Mechanisms at Mach 6*. PhD thesis, University of Delaware, 2019.

[5] Helen Reed, Roger Kimmel, Steven Schneider, Daniel Arnal, Helen Reed, Roger Kimmel, Steven Schneider, and Daniel Arnal. Drag prediction and transition in hypersonic flow. In *28th Fluid Dynamics Conference*, page 1818, 1997.

[6] Joseph J. Kuehl. Thermoacoustic interpretation of second-mode instability. *AIAA Journal*, 56(9):3585–3592, 2018.

[7] Alexander Fedorov. Transition and Stability of High-Speed Boundary Layers. *Annual Review of Fluid Mechanics*, 43(1):79–95, 2011.

[8] A Tumin, E Ulker, and J Klentzman. Boundary-layer solver for binary reacting mixtures of Oxygen and Nitrogen. (February), 2012.

[9] Ernst Heinrich Herschel. *Basics of Aerothermodynamics*. Springer, second edition, 2015.

[10] Jill Klentzman and Anatoli Tumin. The Second Mode in High-enthalpy Boundary Layers in Chemical Non-equilibrium. *Procedia IUTAM*, 14:45–47, 2015.

[11] Joseph Kuehl. Primitive Variable BiGlobal Linear Stability for Compressible Flows. Personal communication, 2020.

[12] Joseph J. Kuehl, Eduardo Perez, and Helen L. Reed. JoKHeR: NPSE simulations of hypersonic crossflow instability. *50th AIAA Aerospace Sciences Meeting Including the New Horizons Forum and Aerospace Exposition*, (January), 2012.

[13] Joseph J. Kuehl. Discrete- and finite-bandwidth-frequency distributions in nonlinear stability applications. *Physics of Fluids*, 29(2), 2017.

[14] Alexander Fedorov and Anatoli Tumin. High-Speed Boundary-Layer instability: Old terminology and a new framework. *AIAA Journal*, 49(8):1647–1657, 2011.

[15] J Klentzman and A Tumin. Stability Code for High Speed Boundary Layers. (August), 2013.

[16] Ernest Bauer. Physics of High-Temperature Air. Part I, Basics. 1990.

[17] Fei Li, Meelan Choudhari, Chau-Lyan Chang, Roger Kimmel, David Adamczak, and Mark Smith. Transition analysis for the ascent phase of hifire-1 flight experiment. *Journal of Spacecraft and Rockets*, 52(5):1283–1293, 2015.